

# TACTILE TOMOGRAPHIC FLUID-FLOW IMAGING WITH A ROBOTIC WHISKER ARRAY

*Cagdas Tuna, Douglas L. Jones, and Farzad Kamalabadi*

Department of Electrical and Computer Engineering and Coordinated Science Laboratory  
University of Illinois at Urbana-Champaign, Urbana, IL 61801, USA

## ABSTRACT

Current sensory array systems do not fully exploit tactile sensing strategies widely used by vibrissal sensing animals to explore their surroundings. We develop a new tactile fluid-flow imaging technique, which relates rat's whisker movements to tomographic imaging to extract fluid-flow characteristics with a robotic whisker array. At high Reynolds numbers, the drag force on a whisker segment is proportional to the relative velocity squared, and acts as a distributed load along the whisker length. Therefore, we propose that it is possible to map out the 2-D cross-sectional mean fluid-flow velocity field with a robotic whisker array by measuring the moment sensed at each whisker base from different directions for tomographic reconstruction. The associated inverse problem for the tomographic image formation is formulated as a MAP estimation problem and solved computationally. The experimental results demonstrate that this new approach offers a fundamentally novel sensor technology for flow-field measurements.

**Index Terms**— Robotic whiskers, tomography, flow imaging, tactile sensing, inverse problem.

## 1. INTRODUCTION

Whisking animals use tactile sensing as a key sensory mechanism for navigation and exploration of their surroundings. Rats can extract object features and discriminate texture through the oscillatory motion of their whiskers [1, 2]. Seals use their whiskers to keep track of hydrodynamic trails generated by fish [3]. Shrews can detect and target their prey in dark with their whiskers [4]. Tactile perception is the principal sensory system particularly for the animals living underground or in muddy, dark environments, where eyesight fails; in other cases, it may also serve as a supplementary information source to other sensory systems such as visual sensing [5].

Biomimetic artificial whisker systems have become an emerging research field in recent years as a result of the expanding neurobiological knowledge about vibrissal sensing of animals. Lungarella *et al.* [6] and Fend *et al.* [7] developed artificial whisker systems based on the power spectral density analysis of the signal measured from whisker sensors

for texture discrimination, inspired by the rat somatosensory system. Pearson *et al.* [8] and Fox *et al.* [9] have constructed advanced active touch robotic systems for shape recognition, texture discrimination and navigation, inspired by the neural-processing of the rat's whisker control. Solomon and Hartmann designed a whisker array for the tactile extraction of three-dimensional object shape by taking lateral slip and surface friction into consideration [10–12]. They also tested two opposing whisker arrays in order to extract the velocity profile of a stream of air moving towards the center of the whisker array, producing single estimates of the flow velocity at a given height, but not reconstructing a full 2-D cross-sectional image of the fluid-flow field [12]. Therefore, the high-resolution recovery of the 2-D cross-section of the mean fluid-flow velocity using tactile sensing remains an important unsolved challenge that would enable an essentially new sensory mechanism for flow-field measurements.

In this paper, we propose a novel tactile flow imaging technique, where we model “whisking” as a tomographic imaging process to extract the 2-D characteristics of the mean fluid-flow. In our recent work, we have introduced the tomography idea with artificial whiskers for object shape recognition using only the angular position at the whisker base during the initial contact with the object, without any need for moment measurements [13]. We now further generalize this approach by developing a more advanced physical model for the imaging of surroundings with artificial whiskers, where we treat the moment measurements at the whisker base on a whisker array as the projections collected at a particular angular view for tomographic reconstruction. The experimental results indicate that our tomographic tactile fluid-flow sensing approach may find a potential use in various robotic applications including underwater tracking, navigation, source localization and obstacle avoidance.

## 2. TACTILE FLUID-FLOW TOMOGRAPHY WITH A ROBOTIC WHISKER ARRAY

Assuming that the robotic whisker is a straight cylindrical beam with substantial stiffness, the equation for the *drag force per unit length*,  $f_D$ , on a circular cylinder is given by

$$f_D = \frac{1}{2}\rho C_D V^2 d, \quad (1)$$

where  $\rho$  is the fluid density, and  $V$  is the relative flow velocity,  $d$  is the diameter of the circular cylinder, and the drag coefficient  $C_D$  is a dimensionless number that depends on the Reynolds number. It has been experimentally shown that the drag coefficient is nearly fixed ( $C_D \approx 1.2$ ) in the range of  $100 < Re < 3 \times 10^5$  for the circular cylinder. Therefore, the drag force on a whisker segment becomes proportional to the square of the relative fluid-flow velocity normal to the whisker segment [14, 15], which acts as a distributed load along the whisker length as illustrated in Figure 1. The distributed load  $p(s)$  on a straight beam can be characterized in terms of the *force per unit length* such that the load applied by the distributed load  $p(s)$  to a small segment of the beam length  $ds$  is  $p(s)ds$  [16]. Assuming the whisker base at the location  $s_0 = 0$ , the incremental moment of  $p(s)$  around the whisker base becomes  $sp(s)ds$ , yielding the moment at the whisker base as

$$M_{base} = \int_0^L sp(s)ds, \quad (2)$$

which can be described as the weighted integral of the distributed load along the whisker of length  $L$ . In tomography, the general goal is to reconstruct a multi-dimensional physical parameter from lower-dimensional measurements [17]. Therefore, if we collect these moment measurements with an array of robotic whiskers from different directions, then we can map out the 2-D cross-sectional fluid-flow velocity field via the tomographic reconstruction.

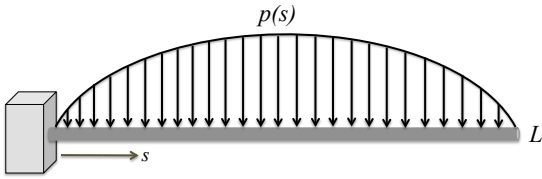


**Fig. 1.** The distributed load along the whisker length: The moment sensed at the whisker base is the weighted integral of the drag force which acts as a distributed load along the whisker length.

In practice, we have to cope with noisy and inaccurate measurements. Self-noise from resistive sensors is known to be approximately Gaussian, since the tomographic measurement is an integral of flow-noise distribution along each whisker. The central limit theorem suggests that the cumulative measurement noise should be approximately Gaussian. Therefore, considering a linear additive Gaussian noise signal model, we can write the linear observation model in the matrix form at the  $i$ th angular view as

$$\mathbf{y}_i = \mathbf{H}_i \mathbf{x}_i + \mathbf{w}_i, \quad (3)$$

where  $\mathbf{x}_i$  is the vector representation of the discretized unknown image field of length  $N$ , and  $\mathbf{y}_i$  is the moment measurement vector of length  $M$ . The linear matrix operator

$\mathbf{H}_i \in \mathbb{R}^{M \times N}$  relates the measurements  $\mathbf{y}_i$  to the unknown image coefficients  $\mathbf{x}_i$  with the additive noise vector  $\mathbf{w}_i$  of length  $M$ .

The resulting inverse problem is the reconstruction of the 2-D cross-sectional fluid-flow characteristics from the 1-D moment measurements. If the unknown flow field is sufficiently static during the measurement interval or it is desired to map out the cross-sectional mean fluid-flow characteristics over a short period of time, the 2-D image can be reconstructed using the measurement set

$$\begin{bmatrix} \mathbf{y}_1 \\ \mathbf{y}_2 \\ \vdots \\ \mathbf{y}_L \end{bmatrix} = \begin{bmatrix} \mathbf{H}_1 \\ \mathbf{H}_2 \\ \vdots \\ \mathbf{H}_L \end{bmatrix} \mathbf{x} + \begin{bmatrix} \mathbf{w}_1 \\ \mathbf{w}_2 \\ \vdots \\ \mathbf{w}_L \end{bmatrix}, \quad (4)$$

where the stationary unknown field  $\mathbf{x}$  has no temporal variation, and  $L$  is the number of angular views used for static reconstruction. Then, the estimate for  $\mathbf{x}$  is found by the measurement vector  $\mathbf{y} = [\mathbf{y}_1^T, \mathbf{y}_2^T, \dots, \mathbf{y}_L^T]^T$  of length  $M \cdot L$  and the forward model matrix  $\mathbf{H} = [\mathbf{H}_1^T, \mathbf{H}_2^T, \dots, \mathbf{H}_L^T]^T \in \mathbb{R}^{M \cdot L \times N}$  along with the known measurement noise vector  $\mathbf{w} = [\mathbf{w}_1^T, \mathbf{w}_2^T, \dots, \mathbf{w}_L^T]^T$  of length  $M \cdot L$ .

The direct inversion of the linear model in Eq. (4) is generally not feasible, since the resulting inverse problem is ill-conditioned and ill-posed, due to the whisker array consisting of only several whiskers and the moment being measured at only a limited number of views [18]. In the Bayesian stochastic framework, if both the unknown image  $\mathbf{x} \sim \mathcal{N}(\boldsymbol{\mu}, \boldsymbol{\Pi})$  and the measurement noise  $\mathbf{w} \sim \mathcal{N}(\mathbf{0}, \mathbf{R})$  are Gaussian, where  $\mathcal{N}(\mathbf{m}, \boldsymbol{\Sigma})$  denotes the Gaussian distribution with mean  $\mathbf{m}$  and covariance  $\boldsymbol{\Sigma}$ , then the MAP estimate  $\hat{\mathbf{x}}_{MAP}$  is

$$\begin{aligned} \hat{\mathbf{x}}_{MAP} &= \arg \max_{\mathbf{x}} \log p(\mathbf{y}|\mathbf{x}) + \log p(\mathbf{x}) \\ &= \arg \min_{\mathbf{x}} \|\mathbf{y} - \mathbf{H}\mathbf{x}\|_{\mathbf{R}^{-1}}^2 + \|\mathbf{x} - \boldsymbol{\mu}\|_{\boldsymbol{\Pi}^{-1}}^2 \end{aligned} \quad (5)$$

where  $\|\mathbf{z}\|_{\mathbf{W}}^2 = \mathbf{z}^T \mathbf{W} \mathbf{z}$  is the weighted residual norm with  $\mathbf{W}$  positive definite. If the unknown image and the measurement noise have non-Gaussian distributions, then the estimate in Eq. (5) becomes the linear minimum mean square error (LMMSE) estimate, which minimizes  $\mathbb{E}[\|\mathbf{x} - \hat{\mathbf{x}}\|_2^2]$ , where  $\mathbb{E}[\cdot]$  is the statistical expectation operator [19]. Taking  $\boldsymbol{\mu} = \mathbf{0}$ , the all-zero vector,  $\mathbf{R} = \lambda \mathbf{I}$ , the  $\lambda$ -scaled identity matrix, and  $\boldsymbol{\Pi} = (\mathbf{D}^T \mathbf{D})^{-1}$  with  $\mathbf{D}$  full column rank, the Eq. (5) yields the Tikhonov-regularized estimate

$$\hat{\mathbf{x}} = \arg \min_{\mathbf{x}} \|\mathbf{y} - \mathbf{H}\mathbf{x}\|_2^2 + \lambda \|\mathbf{D}\mathbf{x}\|_2^2, \quad (6)$$

where the quadratic penalty term refers to the prior knowledge about the unknown fluid-flow field  $\mathbf{x}$  [20, 21]. Using the fact that the fluid-flow velocity field should be fairly smooth except for the cases such as vortex boundaries, the regularization matrix is selected as  $\mathbf{D} = (\mathbf{D}_x^T, \mathbf{D}_y^T)^T$  with  $\mathbf{D}_x$  and  $\mathbf{D}_y$  being the first-order difference approximations to the spatial

derivative operators in the horizontal and vertical directions to impose a specified degree of spatial smoothness, and the regularization parameter  $\lambda$  is used to control the tradeoff between the data fidelity and the amount of smoothness. On the other hand, the Tikhonov-regularized solutions are globally smooth, meaning that the detailed information such as sharp edges are also penalized while suppressing the background noise. Alternatively, other techniques such as the total variation [23] or the maximum entropy regularization [24] may be used to preserve the large gradients in the reconstructed images.

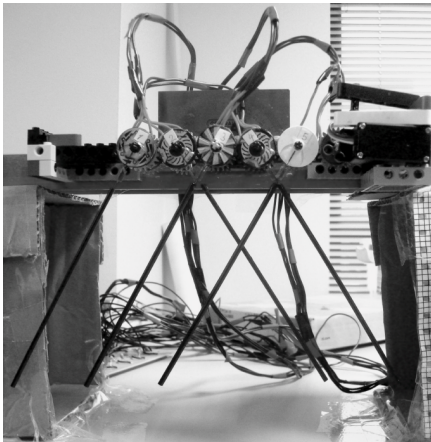


**Fig. 2.** The array of five whiskers used for the 2-D cross-sectional tomographic imaging of the air flow: Each robotic whisker is made up of a superelastic Nitinol wire and covered with a plastic straw to increase the exposure to the flow.

### 3. THE WHISKER ARRAY AND THE CALIBRATION PROCESS

The whisker array built for the 2-D cross-sectional tactile imaging of the different air-flow patterns is shown in Figure 2. Each whisker is made up of a superelastic Nitinol ( $E \approx 8 \times 10^4$  MPa) wire with a diameter of 0.5 mm and length of 15.2 cm covered with a plastic straw to increase the exposure to the flow. The two strain gauges ( $7 \times 4$  mm) facing each other are superglued to the whisker at the whisker base installed 1.5 cm away from the center of rotation. The plastic straw with a diameter of 3 mm and length of 11 cm is superglued onto the Nitinol wire from the tip to the strain gauges, making the whisker more sensitive to small deflections including very small vibrations. The whiskers are attached onto the setup made up of LEGO parts superglued to the carpenter's level of length 24 inches ( $\approx 61$  cm). The whiskers were separated by 2.42 cm apart from each other with three of them (the middle and the two outer whiskers) rotating in one direction while the other two in the opposite direction.

Figure 3 shows the experimental setup for air-flow exper-

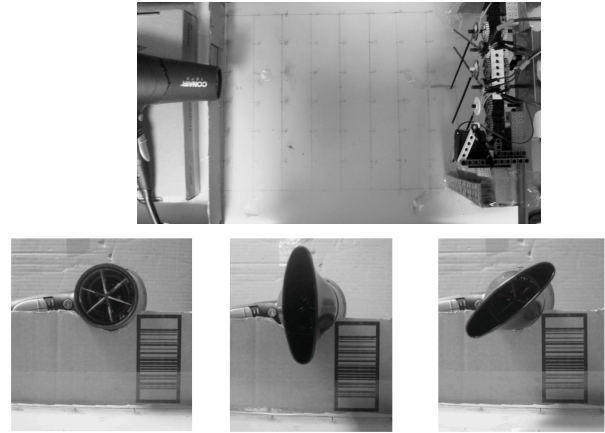


**Fig. 3.** The setup for air flow imaging experiments (top) and the positioning of the the hair dryer to generate different steady air-flow patterns (bottom).

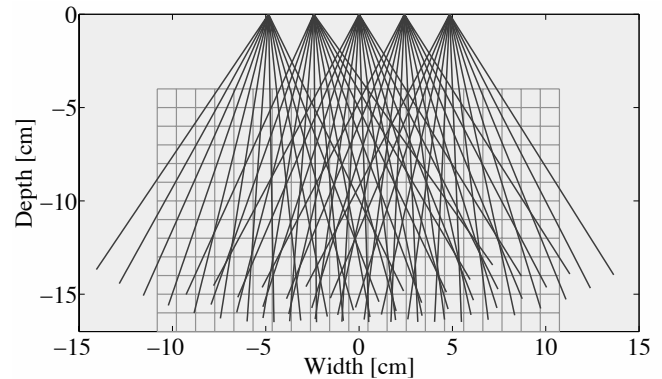


**Fig. 4.** The imaging geometry for the in-air flow imaging experiments: The  $13 \times 21$  grid in the background corresponds to the discretized unknown image field to be reconstructed.

iments, where different steady air-flow patterns were generated by using a hair dryer and a concentrator. As illustrated in Figure 4, a  $13 \times 21$  pixel array is used to discretize the unknown image field, and the whisker array was rotated by  $5^\circ$  normal to the direction of flow between the two successive views using a servomotor. The moment measurements were collected at 13 different angular views, which results in a total number of measurements,  $M = 13 \times 5 = 65$ , at each trial. All of the measured data were low-pass filtered at 160 Hz, sampled at 500 Hz and averaged over 10 seconds.

The ground truth for the air velocity field was determined by moving a hot-wire anemometer along the same  $13 \times 21$  grid used for discretization of the field for each air-flow pattern averaged over three trials. In order to calibrate the physical measurements to the moment sensed at the whisker base, the simulated moment values were obtained over six different ground truth images using the measurement matrix  $\mathbf{H}_{65 \times 273}$  generated with the same angular views from the experiments,

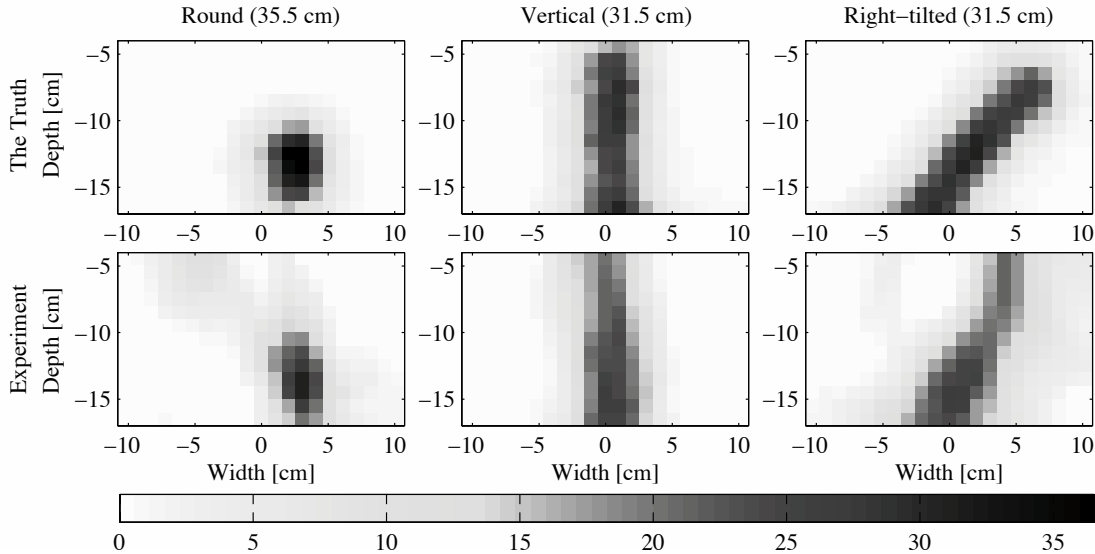


**Fig. 5.** The  $13 \times 21$  velocity-squared static images for the three different steady air-flow patterns generated by the hair dryer: Top row: the ground truth images measured via a hot-wire anemometer. Bottom row: the Tikhonov-regularized images using the calibrated physical measurements.

and the moment measurements were repeated five times for the same flow pattern, totaling  $6 \times 65 = 390$  measurements for each whisker. Then, a second-order polynomial fit to account for any nonlinearity in the measurements was applied for each individual whisker to map the measured voltage to the moment value.

#### 4. EXPERIMENTAL RESULTS

Figure 5 demonstrates the static tactile fluid-flow tomographic imaging results corresponding to the 2-D cross-sectional velocity-squared distribution for the round-shaped, vertical and right-tilted flow shapes generated by positioning the hair dryer as shown in the bottom row of Figure 3. The first row presents the ground truth images for each air-flow shape, whereas the nonnegatively constrained Tikhonov-regularized solutions using the calibrated physical measurements are displayed in the bottom row. The resulting relative error defined as  $\|\mathbf{x}_{GT} - \hat{\mathbf{x}}\|_2 / \|\mathbf{x}_{GT}\|_2$  is also given in Table 1 for each flow pattern. The regularization parameter was manually set to be  $\lambda = 2.5 \times 10^{-10}$  for all of the three cases. There exist, however, techniques such as cross-validation to specify  $\lambda$  based on the available measurements [22]. The resulting images show that the Tikhonov regularization produces stable minimum-norm least squares solutions for the underdetermined system as there are fewer measurements than the number of pixels ( $M < N$ ). The effect of global smoothness can be clearly seen in the resulting images as a relatively large regularization parameter was chosen to alleviate the effects of the background noise, resulting in a larger relative error particularly for the round-shaped and the right-tilted

flow patterns.

Description	Round	Vertical	Right-tilted
Experiment vs. Truth	0.4449	0.1993	0.3556

**Table 1.** The relative error results for the three different steady air-flow patterns generated by the hair dryer.

#### 5. CONCLUSION

The tactile fluid-flow tomographic imaging results strongly demonstrate that integrating tomography into tactile flow sensing with an array of whiskers can recover the mean cross-sectional fluid-flow velocity field with fairly high resolution. To our knowledge, there is no significant work in the signal-processing area on reconstruction of surroundings. Therefore, this new sensing technology may make it possible to perform sophisticated tasks such as the detection of a nearby surface as it alters the flow before the actual whisker contact or tracking a moving object by its wake. Future work includes the extension of our model to a more realistic dynamic tomography scenario, which requires developing a more sophisticated nonstationary image formation model for the tactile fluid-flow tomography with artificial whiskers.

#### 6. ACKNOWLEDGMENTS

The authors would like to thank Joseph H. Solomon and Mitra J. Z. Hartmann for their insightful comments. This research is funded by NSF EFRI-BSBA Award #0938007.

## 7. REFERENCES

- [1] M. Brecht, B. Preilowski, and M. Merzenich, "Functional architecture of the mystacial vibrissae," *Behav Brain Res*, vol. 84, pp. 81–97, 1997.
- [2] M. L. Andermann, J. Ritt, M. A. Neimark, and C. I. Moore, "Neural correlates of vibrissa resonance: band-pass and somatotopic representation of high-frequency stimuli," *Neuron*, vol. 42, pp. 451–463, 2004.
- [3] G. Dehnhardt, B. Mauck, and H. Bleckmann, "Seal whiskers detect water movements," *Nature*, vol. 394, pp. 235–236, July 16 1998.
- [4] F. Anjum, H. Turni, P. G. H. Mulder, J. V. D. Burg, and M. Brecht, "Tactile guidance of prey capture in etruscan shrews," in *Proc. Nat. Acad. Sci. USA*, vol. 103, Oct. 31 2006, pp. 16 544–16 549.
- [5] T. J. Prescott, M. J. Pearson, B. Mitchinson, J. C. W. Sullivan, and A. G. Pipe, "Whisking with robots: From rat vibrissae to biomimetic technology for active touch," *IEEE Robotics and Automation Magazine*, vol. 16, no. 3, pp. 42–50, 2009.
- [6] M. Lungarella, V. V. Hafner, R. Pfeifer, and H. Yokoi, "Artificial whisker sensors in robotics," in *Proceedings of the IEEE/RSJ International Conference on Intelligent Robots and Systems*, 2002, pp. 2931–2936.
- [7] M. Fend, S. Bovet, H. Yokoi, and R. Pfeifer, "An active artificial whisker array for texture discrimination," in *Proceedings of the 2003 IEEE/RSJ Intl. Conference on Intelligent Robots and Systems*, Las Vegas, Nevada, October 2003, pp. 1044–1049.
- [8] M. J. Pearson, B. Mitchinson, J. Welsby, T. Pipe, and T. J. Prescott, "Scratchbot: Active tactile sensing in a whiskered mobile robot," *Lecture Notes in Computer Science (including subseries Lecture Notes in Artificial Intelligence and Lecture Notes in Bioinformatics)*, vol. 6226 LNAI, pp. 93–103, 2010.
- [9] C. W. Fox, M. H. Evans, N. F. Lepora, M. Pearson, A. Ham, and T. J. Prescott, "Crunchbot: A mobile whiskered robot platform," *Lecture Notes in Computer Science (including subseries Lecture Notes in Artificial Intelligence and Lecture Notes in Bioinformatics)*, vol. 6856 LNAI, pp. 102–113, 2011.
- [10] J. H. Solomon and M. J. Z. Hartmann, "Artificial whiskers suitable for array implementation: Accounting for lateral slip and surface friction," *IEEE Transactions on Robotics*, vol. 24, no. 5, pp. 1157–1167, October 2008.
- [11] —, "Extracting object contours with the sweep of a robotic whisker using torque information," *The International Journal of Robotics Research*, vol. 29, no. 9, pp. 1233–1245, August 2010.
- [12] —, "Biomechanics: Robotic whiskers used to sense features," *Nature*, vol. 443, no. 7111, p. 525, 2006.
- [13] C. Tuna, J. H. Solomon, D. L. Jones, and M. J. Z. Hartmann, "Object shape recognition with artificial whiskers using tomographic reconstruction," in *ICASSP, IEEE International Conference on Acoustics, Speech and Signal Processing - Proceedings*, 2012, pp. 2537–2540.
- [14] D. J. Tritton, *Physical Fluid Dynamics*, 2nd ed. New York: Oxford University Press, 1988.
- [15] P. K. Kundu and I. M. Cohen, *Fluid Mechanics*, 3rd ed. London, UK: Elsevier, 2004.
- [16] J. Roy R. Craig, *Mechanics of materials*, 2nd ed. New York: Wiley, 2000.
- [17] F. Kamalabadi, "Multidimensional image reconstruction in astronomy," *IEEE Signal Processing Magazine*, vol. 27, no. 1, pp. 86–96, 2010.
- [18] C. W. Groetsch, *Inverse Problems in the Mathematical Sciences*. Vieweg, 1993.
- [19] S. M. Kay, *Fundamentals of Statistical Signal Processing: Estimation Theory*. Upper Saddle River, NJ: Prentice-Hall, 1993.
- [20] A. Tikhonov, "Solution of incorrectly formulated problems and the regularization method," in *Soviet Math. Doklady*, vol. 4, 1963, pp. 1035–1038.
- [21] W. C. Karl, "Regularization in image restoration and reconstruction," in *Handbook of Image and Video Processing*, A. Bovik, Ed. San Diego: Academic, 2000, pp. 141–160.
- [22] G. H. Golub, M. Heath, and G. Wahba, "Generalized cross-validation as a method for choosing a ridge parameter," *Technometrics*, vol. 21, pp. 215–223, 1979.
- [23] D. M. Strong and T. F. Chan, "Edge-preserving and scale-dependent properties of total variation regularization," in *Inverse Problems*, 2000, pp. 165–187.
- [24] U. Amato and W. Hughes, "Maximum entropy regularization of Fredholm integral equations of the first kind," *Inverse Problems*, vol. 7, pp. 793–808, Dec. 1991.